Imaging gate-tunable Tomonaga-Luttinger liquids in 1H-MoSe₂ mirror twin boundaries

Tiancong Zhu[1,2,†], Wei Ruan[1,2,3,†,*], Yan-Qi Wang[1,2,†], Hsin-Zon Tsai[2], Shuopei Wang[4,5],

Canxun Zhang[2,6], Tianye Wang[1,2], Franklin Liou[2,6], Kenji Watanabe[7], Takashi Taniguchi[8],

Jeffrey B. Neaton[1,2], Alex Weber-Bargioni[1,9], Alex Zettl[2], Ziqiang Qiu[1,2], Guangyu

Zhang[4,5,10], Feng Wang[1,2,6,*], Joel E. Moore[1,2,6,*], Michael F. Crommie[1,2,6,*]

[1]*Materials Sciences Division, Lawrence Berkeley National Laboratory, Berkeley, California 94720, USA*

[2]*Department of Physics, University of California, Berkeley, California 94720, USA*

[3]*Department of Physics, Fudan University, Shanghai 200438, China*

[4]*Beijing National Laboratory for Condensed Matter Physics, Key Laboratory for Nanoscale Physics and Devices, Institute of Physics, Chinese Academy of Sciences, Beijing 100190, China*

[5]*Songshan Lake Materials Laboratory, Dongguan, Guangdong 523808, China*

[6]*Kavli Energy Nano Sciences Institute at the University of California Berkeley and the Lawrence Berkeley National Laboratory, Berkeley, California 94720, USA*

[7]*Research Center for Functional Materials, National Institute for Materials Science, 1-1 Namiki, Tsukuba 305-0044, Japan*

[8]*International Center for Materials Nanoarchitectonics, National Institute for Materials Science, 1-1 Namiki, Tsukuba 305-0044, Japan*

[9]*Molecular Foundry, Lawrence Berkeley National Laboratory, California 94720, USA*

[10]*School of Physical Sciences, University of Chinese Academy of Sciences, Beijing 100190, China*

† These authors contributed equally to this work.

*e-mail: weiruan@fudan.edu.cn, fengwang76@berkeley.edu, jemoore@berkeley.edu, crommie@berkeley.edu

Abstract

One-dimensional electron systems (1DESs) exhibit properties that are fundamentally different from higher-dimensional systems. For example, electron-electron interactions in

1DESs have been predicted to induce Tomonaga-Luttinger liquid behavior. Naturally-occurring grain boundaries in single-layer semiconducting transition metal dichalcogenides provide 1D conducting channels that have been proposed to host Tomonaga-Luttinger liquids, but charge density wave physics has also been suggested to explain their behavior. Clear identification of the electronic ground state of this system has been hampered by an inability to electrostatically gate such boundaries and thereby tune their charge carrier concentration. Here we present a scanning tunneling microscopy/spectroscopy (STM/STS) study of gate-tunable mirror twin boundaries (MTBs) in single-layer $1H$-$MoSe_2$ devices. Gating here enables STM spectroscopy to be performed for different MTB electron densities, thus allowing precise characterization of electron-electron interaction effects. Visualization of MTB electronic structure under these conditions allows unambiguous identification of collective density wave excitations having two distinct velocities, in quantitative agreement with the spin-charge separation predicted by finite-length Tomonaga-Luttinger-liquid theory.

Reduced screening, enhanced quantum fluctuations, and confinement effects in one-dimensional electron systems (1DESs) cause a variety of exotic phenomena such as quantum spin liquids[1], Peierls transitions[2], single electron transport[3], and Tomonaga-Luttinger liquids (TLLs)[4-20]. Important characteristics of TLLs include power-law conductance and spin-charge separation, both of which depend sensitively on the ratio between electron-electron (el-el) interaction strength and electron kinetic energy. Direct, precise measurements of the el-el interaction energy in 1DESs, however, have yet to be reported. The power-law conductance[12-14] and spin-charge separation[15,16,19,20] expected for a TLL in the infinite-length limit have been observed in several 1DESs, but the effects of confinement on finite-length 1DESs are not as well understood. Recently discovered mirror twin boundaries (MTBs) in single-layer (SL) 1H-MoX$_2$ (X = S, Se, Te) provide a one-dimensional (1D) metallic channel embedded in a two-dimensional semiconducting bulk that is ideal for investigating such effects over a range of finite lengths[21]. Signatures of an energy gap as well as charge density modulations in MTBs have been experimentally demonstrated[21-27], consistent with theoretical predictions for a finite-length TLL[28-33], but debate exists as to whether their origin is rather due to a Peierls instability[22,25]. Spectroscopic evidence of spin-charge separation in MTBs has been observed[24], but unambiguous identification of the spin/charge excitations and their velocities is still missing.

Here we report the observation of finite-length TLL behavior in MTBs in gate-tunable SL 1H-MoSe$_2$ devices by means of scanning tunneling microscopy/spectroscopy (STM/STS). This work is different from previous measurements because we have incorporated MTBs into gate-tunable devices that allow us to tune the MTB electron-filling while simultaneously performing atomic-scale characterization of MTB electronic structure. This allows us to unambiguously determine the el-el interaction strength in finite MTBs and to compare this to the MTB electron kinetic energy. This was accomplished by measuring the MTB energy gap

size as a function of applied gate voltage, as well as observing the MTB charge density distribution, both of which are consistent with expectations for a 1D particle-in-a-box with interaction-induced level-splitting. Clear evidence for TLL-based spin-charge separation in MTBs was obtained through observation of two distinct spectral function modulations that correspond to collective spin and charge excitations with separate dispersions. The characteristic TLL parameter obtained from the observed spin and charge velocities was found to be in excellent agreement with the separately measured MTB el-el interaction energy and energy level spacing.

SL 1H-MoSe$_2$ was grown via molecular beam epitaxy at the surface of epitaxial graphene supported by hBN/SiO$_2$/Si (Fig. 1a, Supplementary Fig. 1). This heterostructure allows systematic control of electron-filling at the MoSe$_2$ surface by way of a doped Si bottom gate (Fig. 1b). The device was characterized by STM topographic imaging (Fig. 1a) which shows large SL MoSe$_2$ islands as well as a moiré superlattice formed by alignment of the graphene and hBN[34]. Isolated MTBs and MTB networks are seen as double-straight-line features that exhibit a 4|4P structure as reported previously[21,22] (Fig. 1c).

The electronic properties of an isolated 14-nm long MTB (outlined in yellow in Fig. 1c) was characterized by measuring bias (V_b) dependent STM differential conductance (dI/dV), which reflects the surface electronic local density of states (LDOS). Figure 1d shows a typical dI/dV spectrum at zero gate voltage ($V_g = 0$) that is consistent with previous measurements[22]. Three dominant features in the dI/dV spectrum can be identified: an energy gap of $\Delta_0 \approx 128$ meV bracketing the Fermi level (E_F) (the peak-to-peak width between v_0 and c_0), additional peaks further out in energy from the gap (black arrows labeled by v_1, v_2, c_1, c_2), and a large peak at $V_b \approx -240$ meV (blue arrow).

The spatial distribution of MTB electronic states at the different peak energies was characterized by performing constant-height dI/dV mappings of the MTB in Fig. 1c. Figure

1e shows the electronic LDOS of both the highest occupied state (HOS) at $V_b \approx$ -93 meV (v_0) and the lowest unoccupied state (LUS) at $V_b \approx$ 33 meV (c_0), revealing periodic charge modulations along the MTB. The HOS is observed to have 13 nodes whereas the LUS has 14, as seen from direct comparison of the LDOS line profiles (Fig. 1f) acquired along the orange and green lines in Fig. 1e (nodes here are defined as local minima in the interior of the MTB). A dI/dV map of the v_1 peak exhibits 12 nodes while a map of the c_1 peak exhibits 15 nodes (Supplementary Fig. 2a-c), suggesting a particle-in-a-box nodal progression (i.e., the number of nodes increases by 1 with each higher energy peak). The peaks v_i and c_i ($i \geqslant 0$) can thus be interpreted as representing confined quantum levels. Similar nodal structure was observed in all the MTBs studied here (see Supplementary Fig. 3 for additional representative data).

To gain insight into the nature of the energy gap at E_F we performed STS measurement of the MTB shown in Fig. 1c for different gate voltages in the range -60 V $\leqslant V_g$ $\leqslant$ 60 V, thus enabling the MTB to be tuned from the hole-doped regime (V_g = -60 V) to the electron-doped regime (V_g = 60 V). Figure 2a shows the gate-dependent dI/dV curves acquired at the position marked in Fig. 1e while Fig. 2b shows a dI/dV intensity plot for a finer set of gate voltages at the same position. A key observation here is that the gap-size changes with gate-voltage. The dI/dV spectrum at V_g = -60 V (Fig. 2a, orange) shows a large gap at E_F of $\Delta_{large} \approx$ 121 meV that is similar to the gap, Δ_0, observed at V_g = 0 V (Fig. 2a, red). The dI/dV spectrum at V_g = 60 V (Fig. 2a, blue), however, shows a significantly smaller gap of $\Delta_{small} \approx$ 70 meV. The peaks at the gap-edge of Δ_{small} are also observed to have reduced intensities compared to those bracketing Δ_{large}. As V_g increases from -60 V the overall bandstructure shifts rigidly towards lower energies, consistent with the electrostatic influence of the bottom gate. For $V_g \approx$ 10 V a pronounced peak (blue arrow) appears at negative bias voltage and shifts to higher energies with increasing V_g, opposite to the overall lowering trend seen for the rest of the bandstructure. Such behavior allows us to identify this peak as a tip-

5

induced charging feature of the LUS[35]. For $V_g \approx 20$ V both the charging peak and the LUS

begin to cross E_F, resulting in a transition from the large energy gap to the smaller gap. For

$V_g > 20$ V both the charging peak and the overall bandstructure continues to shift as expected

for increased electron filling of the MTB. Similar gate-dependent behavior was also observed

for 19 other MTBs that were similarly measured using a variety of different STM tips (see

Supplementary Fig. 4 for representative data).

Constant-height dI/dV maps of the HOS and LUS of the MTB in Fig. 1c at $V_g = \pm 60$

V further reveal gate-dependent real-space electronic structure (Fig. 3). The HOS and LUS

for the large gap configuration at $V_g = -60$ V (Δ_{large}) exhibit 13 nodes and 14 nodes,

respectively (Fig. 3b), consistent with the real-space electronic structure observed for the

undoped ($V_g = 0$ V) case (Fig. 1e, f). The HOS and LUS for the small gap configuration at V_g

$= 60$ V (Δ_{small}), on the other hand, both exhibit 14 nodes (Fig. 3e). The LDOS maps of higher

energy peaks are summarized in Supplementary Fig. 2d-i. (Similar gate-dependent nodal

structure was observed for 9 MTBs).

In order to characterize the energy- *and* momentum-resolved MTB electronic

structure we measured dI/dV spectra along an MTB for the large gap case ($V_g = 0$V) (Fig. 4a)

and performed Fourier transform (FT) analysis of the resulting density plot (here we chose a

longer MTB than that in Figs. 1-3 to achieve better momentum resolution). Figure 4b shows

the energy-dependence of the STS intensity plot as a function of the MTB axial coordinate (x

axis) and the sample bias (y axis). Fast real-space modulations ($\lambda \sim 1$ nm) create a complex

MTB nodal structure that coexists with a longer wavelength modulation that induces a dome-

shaped charge density profile (similar real-space modulations in electronic structure have

been previously reported both for MTBs[19,21] and carbon nanotubes[15,16]). Figure 4c shows the

corresponding FT of the STS intensity plot, revealing both the energy- and momentum-

dependence of the electronic structure. Two linear dispersion branches with different slopes

are seen to cross E_F at $q/2\pi \approx 1$ nm^{-1} (which we identify as $q = 2k_F$ where k_F is the Fermi

wavevector) and are labeled by blue and red markers in Fig. 4c. These branches correspond

to "fast" real-space nodal structure and are dubbed the "fast branches" hereafter. The velocity

of the blue branch is 3.5×10^5 m/s (extracted from twice the slope of the dispersion since

LDOS $\propto |\psi(x)|^2$) and is consistent with the Fermi velocity, v_F, of the MTB metallic

bandstructure[22,24]. The velocity of the red branch, on the other hand, is 6.5×10^5 m/s and is

significantly higher than v_F. An additional linear branch near the Γ point (labeled by orange

markers in Fig. 4c) can be resolved that corresponds to the long wavelength modulation

mentioned above (and is dubbed the "slow branch" hereafter). The existence of multiple

linear dispersion branches causes blurring of the real-space nodal structure at peak energies

far from E_F (Supplementary Fig. 3). A static mode (i.e., constant wavevector with energy) at

$q = 2k_F$ can also be observed, consistent with previous results[22]. Fig. 4d provides a 2nd

derivative plot of the data presented in Fig. 4c which allows the various dispersive features to

be more clearly seen. This type of behavior was observed in all 7 of the MTBs that were

characterized in this way (see Supplementary Fig. 5 for additional representative data). All

the measured MTBs were well isolated from other MTBs and defects to avoid spatial

inhomogeneities in the local electrostatic environment that might obscure the intrinsic MTB

behavior.

Our experimental results are in excellent agreement with the theoretical predictions

for a confined TLL. Our observation of gate-induced modulation of the energy gap size

reveals the strength of el-el Coulomb repulsion in a MTB and thus confirms that they should,

indeed, be described by TLL theory. Were el-el interactions absent then the Fermi-level

energy gap would be gate-independent and would simply equal the 1D single-particle level-

spacing value of $E_0 = h v_F \pi / L$. The presence of el-el Coulomb repulsion explains the large and

small gap variation seen for different electron fillings since each MTB quantum confinement

level has spin degeneracy and can accept two electrons. When one of the spin states is filled by tuning the gate voltage then el-el repulsion will create a charging gap $\Delta_{\text{small}} = E_C$ that is required to inject a second electron with the opposite spin into the same MTB level, resulting in level splitting and a magnetic ground state (Fig. 3f, green). This explains the identical real-space nodal structure experimentally observed for the HOS and LUS in Fig. 3e, as well as the reduced spectral weight of the HOS/LUS states in Fig. 2 at $V_g = 60$ V (where the HOS and LUS both contain just a single spin state) compared to $V_g = -60$ V (where the HOS and LUS are both spin degenerate). When the MTB HOS level contains two electrons (e.g., at $V_g = -60$ V) then repulsion between the HOS and LUS electrons adds E_C to the single-particle level-spacing, E_0, resulting in a larger gap $\Delta_{\text{large}} = E_0 + E_C$ (Fig. 3c). In this case we expect a different number of nodes for the HOS and LUS since they are associated with different quantum confinement levels, as seen experimentally in Fig. 3b. This scenario is also supported by the fact that the single-particle level-spacing defined by the energy difference between v_1 and the HOS (e.g., $E_0 = 52$ meV (Fig. 1d)) matches the value estimated from a different set of levels by $E_0 = \Delta_{\text{large}} - \Delta_{\text{small}}$ (e.g., 51 meV (Fig. 2a)).

Our observation of gate-induced modulation of the MTB energy gap allows a direct and precise measurement of E_C/E_0, the ratio of MTB el-el interaction energy to electron kinetic energy. Since the single-particle level-spacing can be expressed as $E_0 = h v_F \pi / L$ and the charging energy E_C is inversely proportional to the separation of two electrons, $\langle x_1 - x_2 \rangle \sim L$, we expect both Δ_{large} and Δ_{small} to scale as L^{-1}. This is confirmed by measurements of the gap-size statistics for MTBs of different lengths ranging from 6 nm to 30 nm (Fig. 5a). The ratio of E_C/E_0 is thus observed to be universal for MTBs of different lengths. This ratio is related to TLL behavior through the TLL parameter K_c as[12,31]

$$K_c = \left(1 + \frac{2E_C}{E_0}\right)^{-\frac{1}{2}} \tag{1}$$

(see Supplementary Note 1.1). The energy gaps measured in our spectroscopy of MTBs having different lengths yield a universal value of $K_c = 0.54 \pm 0.03$ (Fig. 5b).

Another piece of evidence supporting the TLL interpretation of MTBs is the observation of spin-charge separation. The existence of two linear fast branches in the FT-STS suggests that a single metallic band picture[22,24] for MTBs is insufficient, whereas TLL-based spin-charge separation can explain this quantitatively. To see this we performed simulations of the expected LDOS for a finite 1D TLL[24,32] having $K_c = 0.54$ (Fig. 4e-g) and with all other material-dependent parameters constrained by experimental values (see Supplementary Note 1.2). Both the fast and slow modulations can be seen in the resulting theoretical energy-dependent LDOS (Fig. 4e), which closely resembles the experimental features seen in Fig. 4b. Clear spin-charge separation can be observed in the FT of the simulated LDOS, as seen in Fig. 4f where two linear branches show LDOS modulations induced by spin (blue arrow) and charge (red arrow) density excitations that have distinct velocities[24,28,32,33] (the slow branch and static $2k_F$ branch can also both be seen). Direct comparison between Fig. 4c and Fig. 4f allows us to identify the blue and red branches in the experimental data of Fig. 4c as the TLL spin and charge branches, respectively (this can be seen even better by comparing the second derivative dispersions in Figs. 4d and 4g). The clear signature of spin-charge separation seen in the FT-STS measurement allows us to experimentally extract the TLL parameter through a second, independent method via the following relation:[8,9,15,16,29,30,36]

$$K_c = \frac{v_s}{v_c}, \tag{2}$$

where v_s and v_c are the slopes (i.e., velocities) of the spin and charge branches, respectively (Supplementary Note 1.1). This technique yields a value of $K_c = 0.53 \pm 0.05$ (Fig. 5c), in excellent agreement with the value of $K_c = 0.54 \pm 0.03$ determined from the energy gap ratio E_C/E_0 (Fig. 5b). The TLL picture is thus confirmed through self-consistent measurements of

9

both energy level alignment (Fig. 2) and spatial LDOS modulations (Fig. 4).

In conclusion, our observation of gate-dependent energy gaps via STS allows precise measurement of the el-el Coulomb interaction energy in 1D MTBs. Spin-charge separation visualized via FT-STS allows us to confirm that this interaction indeed leads to TLL behavior, including distinct spin and charge velocities. The TLL parameter determined separately from the el-el interaction energy and spin/charge velocities are both in excellent agreement with each other. Our experiment demonstrates that combining STM with gate-tunable single-layer devices is a useful approach for gaining a better understanding of electron correlation effects in nanoscale systems. Our device thus provides an ideal platform to study the response of 1D TLL systems to magnetic scatterers[37,38], external magnetic field[39], and tuned dielectric environments[26].

Acknowledgments

Author Contributions:

T.Z., W.R., F.W., and M.F.C. initiated and conceived this project. W.R., T.Z., and C.Z. carried out STM/STS measurements under the supervision of M.F.C. Y.-Q.W. and W.R. performed theoretical analysis and numerical calculation under the supervision of J.E.M. T.Z. and T.W. performed MBE growth under the supervision of Z.Q. H.-Z.T. and F.L. performed device fabrication under the supervision of M.F.C. and A.Z. S.W. prepared epitaxial graphene under the supervision of G.Z. K.W. and T.T. synthesized hBN crystals. T.Z., W.R., J.B.N., A.W.-B., F.W. and M.F.C. analyzed the experimental data. T.Z., W.R., Y.-Q.W., and M.F.C. wrote the manuscript with the help from all authors. All authors contributed to the scientific discussion.

Competing interests:

The authors declare no competing interests.

Methods

Sample fabrication

The preparation of the epitaxial graphene/hBN heterostructure supported on SiO_2/Si substrate is described in ref.[34]. Single-layer 1H-$MoSe_2$ films with MTBs were grown directly on epitaxial graphene/hBN heterostructures using MBE. Mo and Se were evaporated from an e-beam evaporator and a home-built Knudsen cell, respectively. The flux ratio between Mo and Se was ~ 1:100 and the sample was kept at 450 $^{\circ}$C during the growth. After growth the sample was heated up to ~600 $^{\circ}$C and annealed under Se for 30 min. The sample was capped with ~20 nm of amorphous Se before being taken out of the ultrahigh-vaccum (UHV) growth chamber. Electrical contacts were made by depositing Cr/Au (3 nm/30 nm) through a shadow mask.

STM/STS measurements

Scanning tunneling miscroscopy/spectroscopy (STM/STS) measurements were

performed in a low-temperature UHV STM system (CreaTec) at $T = 5$ K. Prior to

measurements the samples were annealed in UHV at ~200 °C for 1 hour to remove the Se

capping layers and then immediately transferred in situ to the STM stage at $T = 5$ K.

Electrochemically etched tungsten tips were calibrated on a Au(111) surface before other

measurements. dI/dV spectra were collected using standard lock-in techniques ($f = 401$ Hz).

dI/dV mapping was performed in constant-height mode (i.e., with the feedback loop open).

Data availability:

The data that support the findings of this study are available from the corresponding

authors upon reasonable request.

Code availability:

The codes used in this study are available from the corresponding author upon

reasonable request.

References

1   Kim, B. J., Koh, H., Rotenberg, E., Oh, S.-J., Eisaki, H., Motoyama, N., Uchida, S., Tohyama, T., Maekawa, S., Shen, Z.-X. & Kim, C. Distinct spinon and holon dispersions in photoemission spectral functions from one-dimensional $SrCuO_2$. *Nat. Phys.* **2**, 397-401 (2006).
2   Grüner, G. The dynamics of charge-density waves. *Rev. Mod. Phys.* **60**, 1129-1181 (1988).
3   Bockrath, M., Cobden, D. H., McEuen, P. L., Chopra, N. G., Zettl, A., Thess, A. & Smalley, R. E. Single-Electron Transport in Ropes of Carbon Nanotubes. *Science* **275**, 1922-1925 (1997).
4   Tomonaga, S.-i. Remarks on Bloch's Method of Sound Waves applied to Many-Fermion Problems. *Prog. Theor. Phys.* **5**, 544-569 (1950).
5   Luttinger, J. M. An Exactly Soluble Model of a Many-Fermion System. *J. Math. Phys.* **4**, 1154-1162 (1963).
6   Mattis, D. C. & Lieb, E. H. Exact Solution of a Many-Fermion System and Its Associated Boson Field. *J. Math. Phys.* **6**, 304-312 (1965).
7   Haldane, F. D. M. 'Luttinger liquid theory' of one-dimensional quantum fluids. I. Properites of the Luttinger model and their extension to the general 1D interacting spinless Fermi gas. *J. Phys. C: Solid State Phys.* **14**, 2585-2609 (1981).
8   Gogolin, A. O., Nersesyan, A. A. & Tsvelik, A. M. *Bosonization and Strongly Correlated Systems.* (Cambridge University Press, 1998).
9   Giamarchi, T. *Quantum Physics in One Dimension.* (Oxford University Press, 2004).
10   Matveev, K. A., Furusaki, A. & Glazman, L. I. Bosonization of strongly interacting one-dimensional electrons. *Phys. Rev. B* **76**, 155440 (2007).

11   Ilan, R., Cayssol, J., Bardarson, J. H. & Moore, J. E. Nonequilibrium transport through a gate-controlled barrier on the quantum spin Hall edge. *Phys. Rev. Lett.* **109**, 216602 (2012).

12   Bockrath, M., Cobden, D. H., Lu, J., Rinzler, A. G., Smalley, R. E., Balents, L. & McEuen, P. L. Luttinger-liquid behaviour in carbon nanotubes. *Nature* **397**, 598-601 (1999).

13   Yao, Z., Postma, H. W. C., Balents, L. & Dekker, C. Carbon nanotube intramolecular junctions. *Nature* **402**, 273-276 (1999).

14   Ishii, H., Kataura, H., Shiozawa, H., Yoshioka, H., Otsubo, H., Takayama, Y., Miyahara, T., Suzuki, S., Achiba, Y., Nakatake, M., Narimura, T., Higashiguchi, M., Shimada, K., Namatame, H. & Taniguchi, M. Direct observation of Tomonaga-Luttinger-liquid state in carbon nanotubes at low temperatures. *Nature* **426**, 540-544 (2003).

15   Lee, J., Eggert, S., Kim, H., Kahng, S. J., Shinohara, H. & Kuk, Y. Real space imaging of one-dimensional standing waves: direct evidence for a Luttinger liquid. *Phys. Rev. Lett.* **93**, 166403 (2004).

16   Shi, Z., Hong, X., Bechtel, H. A., Zeng, B., Martin, M. C., Watanabe, K., Taniguchi, T., Shen, Y.-R. & Wang, F. Observation of a Luttinger-liquid plasmon in metallic single-walled carbon nanotubes. *Nat. Photon.* **9**, 515-519 (2015).

17   Chang, A. M. Chiral Luttinger liquids at the fractional quantum Hall edge. *Rev. Mod. Phys.* **75**, 1449-1505 (2003).

18   Stühler, R., Reis, F., Müller, T., Helbig, T., Schwemmer, T., Thomale, R., Schäfer, J. & Claessen, R. Tomonaga–Luttinger liquid in the edge channels of a quantum spin Hall insulator. *Nat. Phys.* **16**, 47-51 (2019).

19   Auslaender, O. M., Steinberg, H., Yacoby, A., Tserkovnyak, Y., Halperin, B. I., Baldwin, K. W., Pfeiffer, L. N. & West, K. W. Spin-Charge Separation and Localization in One Dimension. *Science* **308**, 88-92 (2005).

20   Jompol, Y., Ford, C. J. B., Griffiths, J. P., Farrer, I., Jones, G. A. C., Anderson, D., Ritchie, D. A., Silk, T. W. & Schofield, A. J. Probing Spin-Charge Separation in a Tomonaga-Luttinger Liquid. *Science* **325**, 597-601 (2009).

21   Batzill, M. Mirror twin grain boundaries in molybdenum dichalcogenides. *J. Phys.: Condens. Matter* **30**, 493001 (2018).

22   Barja, S., Wickenburg, S., Liu, Z.-F., Zhang, Y., Ryu, H., Ugeda, M. M., Hussain, Z., Shen, Z.-X., Mo, S.-K., Wong, E., Salmeron, M. B., Wang, F., Crommie, M. F., Ogletree, D. F., Neaton, J. B. & Weber-Bargioni, A. Charge density wave order in 1D mirror twin boundaries of single-layer $MoSe_2$. *Nat. Phys.* **12**, 751-757 (2016).

23   Ma, Y., Diaz, H. C., Avila, J., Chen, C., Kalappattil, V., Das, R., Phan, M. H., Cadez, T., Carmelo, J. M., Asensio, M. C. & Batzill, M. Angle resolved photoemission spectroscopy reveals spin charge separation in metallic $MoSe_2$ grain boundary. *Nat. Commun.* **8**, 14231 (2017).

24   Jolie, W., Murray, C., Weiß, P. S., Hall, J., Portner, F., Atodiresei, N., Krasheninnikov, A. V., Busse, C., Komsa, H.-P., Rosch, A. & Michely, T. Tomonaga-Luttinger Liquid in a Box: Electrons Confined within MoS_2 Mirror-Twin Boundaries. *Phys. Rev. X* **9**, 011055 (2019).

25   Wang, L., Wu, Y., Yu, a., Chen, A., Li, H., Ren, W., Lu, S., Ding, S., Yang, H., Xue, Q.-K., Li, F.-S. & Wang, G. Direct Observation of One-Dimensional Peierls-type Charge Density Wave in Twin Boundaries of Monolayer $MoTe_2$. *ACS Nano* **14**, 8299-8306 (2020).

26   Xia, Y., Zhang, J., Jin, Y., Ho, W., Xu, H. & Xie, M. Charge Density Modulation and the Luttinger Liquid State in $MoSe_2$ Mirror Twin Boundaries. *ACS Nano* **14**, 10716-

10722 (2020).

27 Yang, X., Wang, H., Xian, J.-J., Meng, S., Nagaosa, N., Zhang, W.-H., Liu, H.-W., Ling, Z.-H., Fan, K., Zhang, Z.-M., Qin, L., Zhang, Z.-H., Liang, Y. & Fu, Y.-S. Manipulating Hubbard-type Coulomb blockade effect of metallic wires embedded in an insulator. *arXiv* **2104.08577** (2021).

28 Fabrizio, M. & Gogolin, A. O. Interacting one-dimensional electron gas with open boundaries. *Phys. Rev. B* **51**, 17827-17841 (1995).

29 Eggert, S., Johannesson, H. & Mattsson, A. Boundary Effects on Spectral Properties of Interacting Electrons in One Dimension. *Phys. Rev. Lett.* **76**, 1505-1508 (1996).

30 Mattsson, A. E., Eggert, S. & Johannesson, H. Properties of a Luttinger liquid with boundaries at finite temperature and size. *Phys. Rev. B* **56**, 15615-15628 (1997).

31 Kane, C., Balents, L. & Fisher, M. P. A. Coulomb Interactions and Mesoscopic Effects in Carbon Nanotubes. *Phys. Rev. Lett.* **79**, 5086-5089 (1997).

32 Anfuso, F. & Eggert, S. Luttinger liquid in a finite one-dimensional wire with box-like boundary conditions. *Phys. Rev. B* **68**, 241301 (2003).

33 Kakashvili, P., Johannesson, H. & Eggert, S. Local spectral weight of a Luttinger liquid: Effects from edges and impurities. *Phys. Rev. B* **74**, 085114 (2006).

34 Yang, W., Chen, G., Shi, Z., Liu, C.-C., Zhang, L., Xie, G., Cheng, M., Wang, D., Yang, R., Shi, D., KenjiWatanabe, Taniguchi, T., Yao, Y., Zhang, Y. & Zhang, G. Epitaxial growth of single-domain graphene on hexagonal boron nitride. *Nat. Mater.* **12**, 792-797 (2013).

35 Brar, V. W., Decker, R., Solowan, H.-M., Wang, Y., Maserati, L., Chan, K. T., Lee, H., Girit, Ç. O., Zettl, A., Louie, S. G., Cohen, M. L. & Crommie, M. F. Gate-controlled ionization and screening of cobalt adatoms on a graphene surface. *Nat. Phys.* **7**, 43-47 (2011).

36 Miranda, E. Introduction to Bosonization. *Brazilian Journal of Physics* **33**, 3-35 (2003).

37 Lee, D. H. & Toner, J. Kondo effect in a Luttinger liquid. *Phys. Rev. Lett.* **69**, 3378-3381 (1992).

38 Furusaki, A. & Nagaosa, N. Kondo effect in a Tomonaga-Luttinger liquid. *Phys. Rev. Lett.* **72**, 892-895 (1994).

39 Hikihara, T., Furusaki, A. & Matveev, K. A. Renormalization of impurity scattering in one-dimensional interacting electron systems in magnetic field. *Phys. Rev. B* **72**, 035301 (2005).
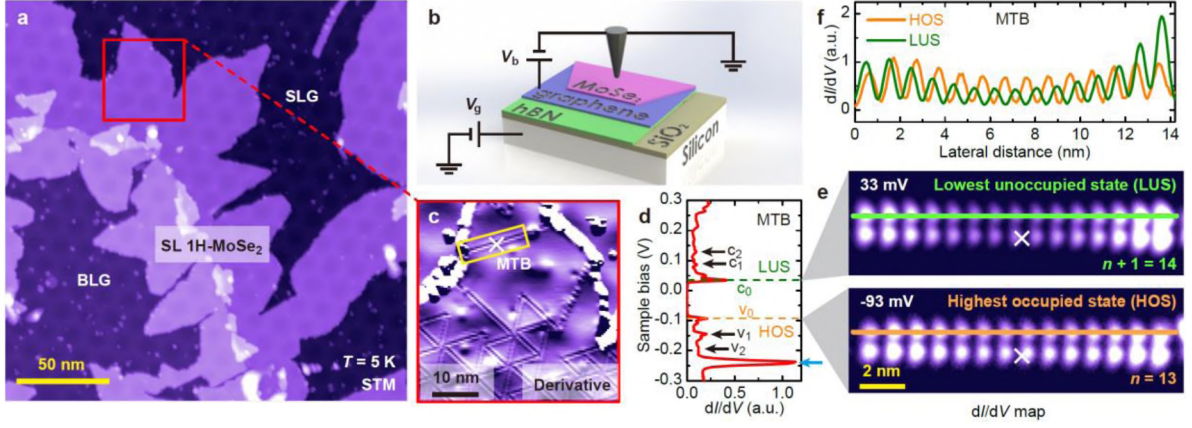
**Fig. 1. STM characterization of a SL MoSe₂/Graphene/hBN/SiO₂/Si device at T = 5 K.**

a, Large-scale STM topography of a single-layer MoSe₂/Graphene/hBN/SiO₂/Si device (V_b = -2 V, I_t = 10 pA). **b**, Schematic of the experimental device setup. **c**, A close-up STM derivative image of the mirror twin boundaries (MTBs) in the area indicated by a red square in **a** (the derivative plot enhances the MTB image contrast). **d**, dI/dV spectrum acquired on the MTB in the yellow rectangle in **c** at the position marked by a white cross (V_b = -0.3 V, I_t = 100 pA, V_{mod} = 2 mV). The energy gap is bracketed by the highest occupied state (HOS, v_0) and the lowest unoccupied state (LUS, c_0). Other 1D quantum well states are labeled with black arrows while a charging peak is labeled with a blue arrow. **e**, Constant-height dI/dV maps of the MTB in **c** taken at the LUS (top) and the HOS (bottom) (V_{mod} = 10 mV). The HOS map exhibits 13 nodes while the LUS map exhibits 14 nodes. **f**, LDOS line profiles of the MTB at the energies of both the LUS and the HOS, acquired along the orange and the green lines in **e**.

15
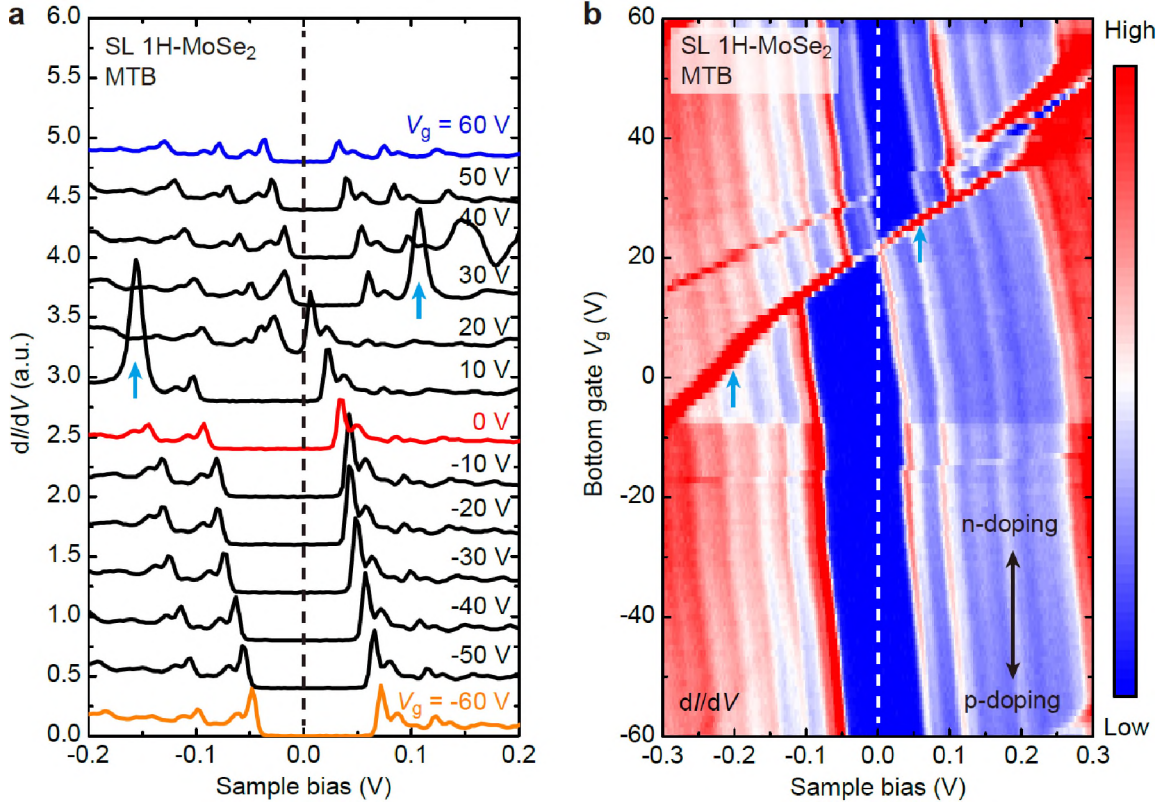
**Fig. 2. Gate dependent electronic structure of the MTB.**

a, A waterfall plot showing dI/dV spectra acquired over the gate voltage range -60 V $\leqslant$ V_g $\leqslant$ 60 V on the MTB from Fig. 1c (V_b = -0.3 V, I_t = 100 pA, V_{mod} = 2 mV, position marked in Fig. 1c). The spectra exhibit a large energy gap for V_g < 20 V and a small gap for V_g > 20 V. Electronic structure shifts to lower energy with increasing V_g (i.e., with increased electron doping). **b**, A density plot of dI/dV spectra acquired for -60 V $\leqslant$ V_g $\leqslant$ 60 V on the MTB showing the overall bandstructure shift and energy gap transition as a function of V_g (V_b = -0.3 V, I_t = 100 pA, V_{mod} = 5 mV).
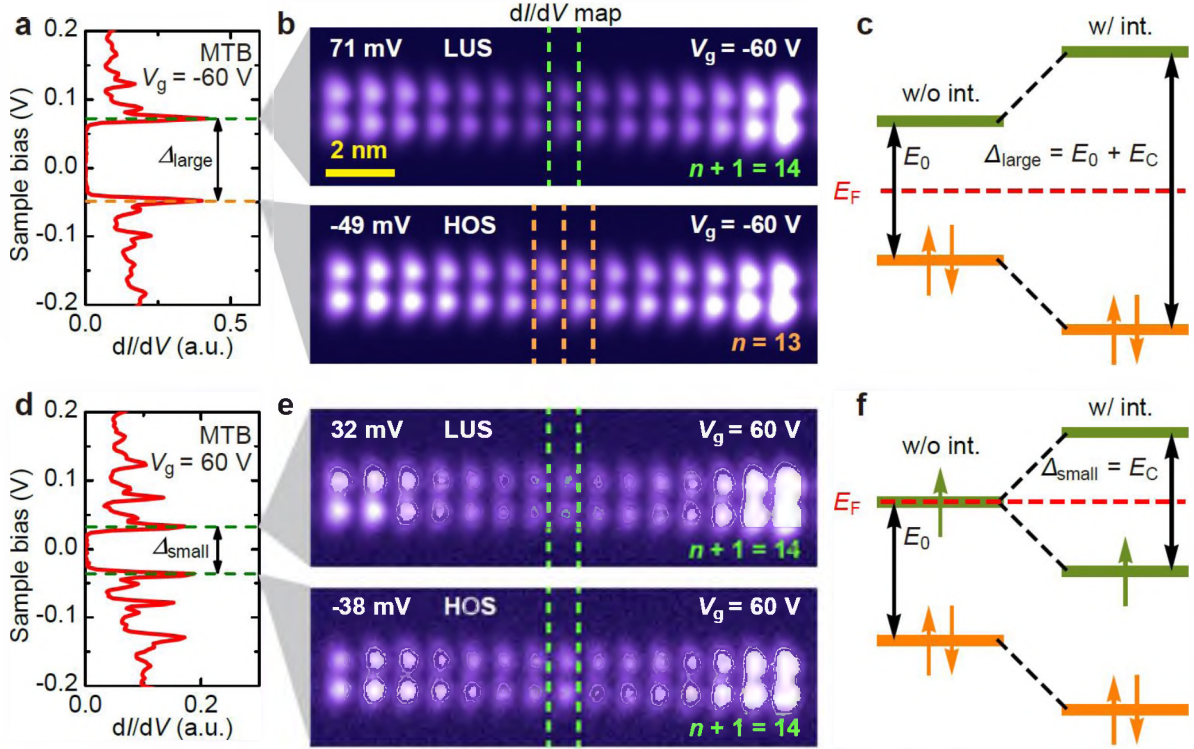
Fig. 3. Electronic LDOS maps of states at gap edges for V_g = -60 V and V_g = 60 V.

a, dI/dV spectrum of the MTB in Fig. 1c taken at V_g = -60 V shows a large energy gap (V_b = -0.3 V, I_t = 100 pA, V_{mod} = 2 mV, position marked in Fig. 1c). **b**, Constant-height dI/dV maps of states at gap edges for V_g = -60 V (V_{mod} = 10 mV). The number of nodes for the HOS and the LUS differ by one. **c**, Energy level diagram for the large energy gap case with and without el-el interactions. **d**, dI/dV spectrum of the same MTB taken at V_g = 60 V shows a small energy gap (V_b = -0.3 V, I_t = 100 pA, V_{mod} = 2 mV, same position). **e**, Constant-height dI/dV maps of states at the gap edges for V_g = 60 V (V_{mod} = 10 mV). The number of nodes for the HOS and the LUS are now the same. **f**, Energy level diagram for the small energy gap case with and without el-el interactions.

17
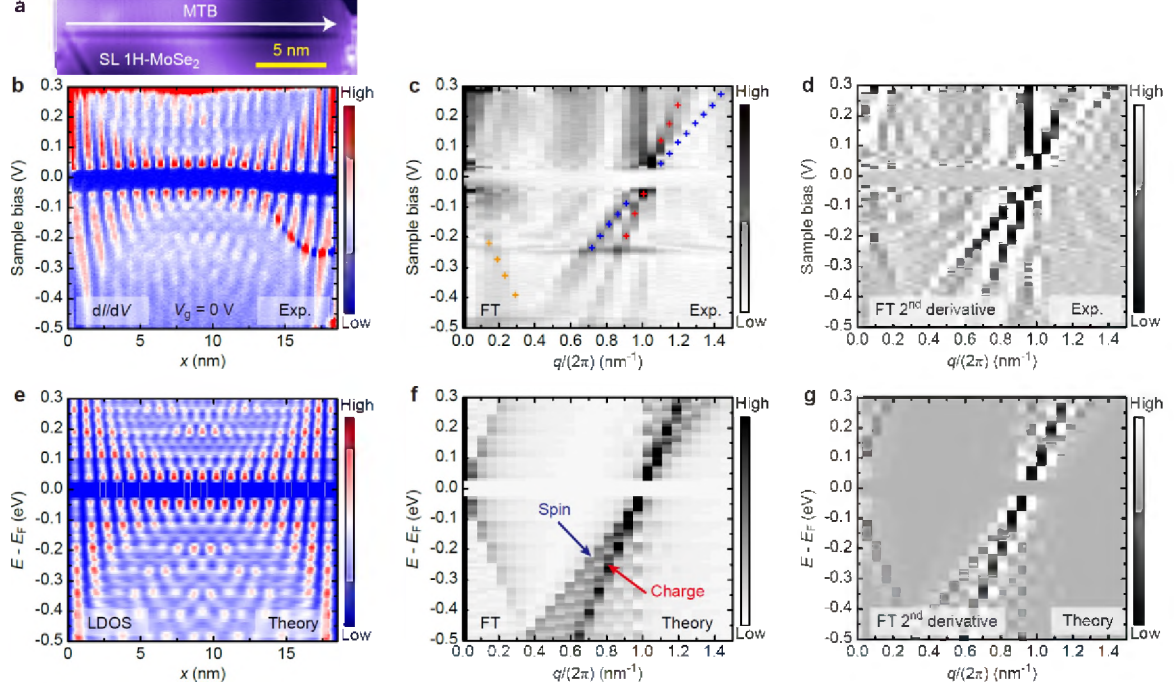
Fig. 4. Experimental STS along MTB at V_g = 0 V compared to theoretical LDOS based on TLL model.

a, STM topography of an 18-nm long MTB (V_b = -2 V, I_t = 10 pA). **b**, dI/dV intensity plot of the MTB along the white arrow in **a** as a function of sample bias V_b (V_{mod} = 5 mV, tip positioning parameters: V_b = -0.6 V, I_t = 100 pA). **c**, Fourier transform (FT) of the dI/dV data in **b** as a function of V_b and wavevector q. Main features include two linear fast branches with different velocities (marked blue and red), a slow branch near the Γ point (orange dashed line), and a static branch with energy-independent wavevector at $q/2\pi \approx 1$ nm^{-1} (= $2k_F/2\pi$). **d**, Second-derivative plot of FT in **c** enhances image contrast of the spectral features. **e**, Theoretical LDOS predicted by the finite TLL model using E_{gap} = 0.08 eV, K_c = 0.54, K_s = 1, $k_F^+ = 19\pi/L$, $k_F^- = 18\pi/L$, $v_c\pi/L$ = 0.073 eV, and $v_s\pi/L$ = 0.039 eV. **f**, FT of the theoretical LDOS in **e** shows similar dispersive and static branches as the experimental data in **c**. **g**, Second-derivative plot of the theoretical FT in **f** for comparison to experimental data in **d**.

18
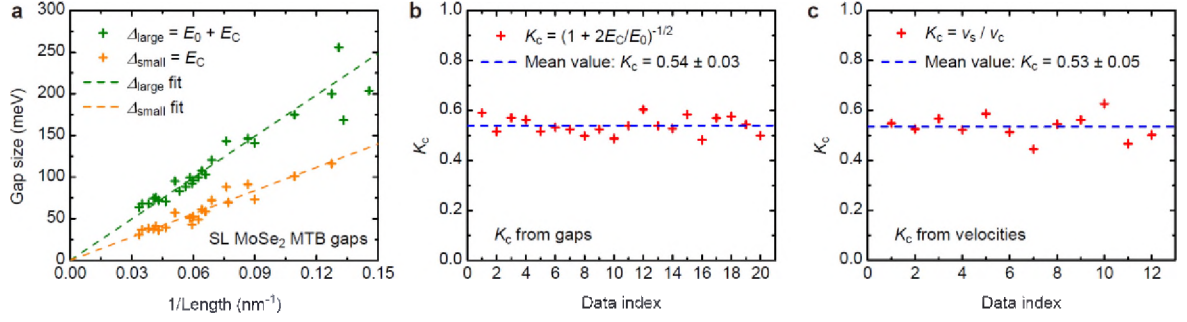
Fig. 5. Gap-size statistics and MTB TLL parameter obtained in two different ways.

a, Measured large (green) and small (orange) energy gaps for MTBs of different lengths. Both types of gap scale in size as $1/L$ where L is the MTB length. The dashed lines represent linear fits to the data. **b**, The TLL parameter obtained from the measured charging energy, E_C, and single-particle level spacing, E_0, for MTBs having different lengths ($K_c = 0.54 \pm 0.03$). **c**, The TLL parameter obtained from the ratio of the measured spin and charge velocities for MTBs having different lengths ($K_c = 0.53 \pm 0.05$). The excellent agreement between the K_c values obtained using these two different experimental techniques provides strong evidence for TLL behavior in SL MoSe$_2$ MTBs.